Bimodal Resonance Phenomena. Part III: High-Contrast Grating Reflectors

Bimodal Resonance Phenomena. Part III: High-Contrast Grating Reflectors

Alberto Tibaldi, Pierluigi Debernardi, and Renato Orta, *Senior Member, IEEE*

***Abstract*—The extraordinary broadband high-reflectivity features of high-contrast gratings are stimulating great interest in many opto-electronic applications. In view of obtaining a simple simulation framework, the analogy of high-contrast grating reflectors with bimodal Fabry-Pérot interferometers is proposed. The closed-form expressions of the interferometer reflectivity, obtained starting from a novel parametrization of the scattering matrices characterizing the bar-air interface, allow a complete exploration of the device parameter space, explaining and predicting the phenomenon of ultra-broadband quasi-100% reflectivity. In this paper an optimized and numerically efficient design procedure is described and compared with the standard rigorous coupled wave analysis, both for the classical "bar-in-air" configuration and for a more robust and practical one, with bars lying on a dielectric support. It is shown that the model can be applied also in the more realistic case of lossy gratings.**

***Index Terms*—Gratings, Fabry-Pérot interferometers**

I. Introduction

HIGH-Contrast Gratings (HCGs) have attracted the interest of many research groups worldwide. Even if they might have a strong impact in several optoelectronic devices [1], [2], [3], their main application has been so far focused on vertical-cavity surface-emitting lasers (VCSELs) [1], [4], [5], [6], [7]. Such compact, reliable and low cost semiconductor devices are nowadays the optical sources of choice in almost all Information Technology applications, such as mice, gas sensors, transceivers, 3D cameras, etc [8].

In today's commercial VCSELs, more than 95% of the semiconductor material is used for the distributed Bragg mirrors (DBRs). Because of the very small active region (few quantum wells), the reflectivity must be higher than 99%, which requires typically about 30 quarter-wavelength pairs in AlGaAs-based VCSELs.

A lot of research is ongoing on tunable VCSELs for their wide range of possible applications: WDM datacom, wavelength reconfigurable distribution networks, optical spectrometry for sensing, optical tomography for biomedical applications (*e.g.* skin cancer detection or ophthalmic applications [9]) are some examples. Very high tuning ranges have been already achieved [10], based on a coupled-cavity scheme with an airgap, which is varied for the tuning. In such devices the mass of the movable mirror could be an issue, if fast electrostatic actuation is adopted [11]. Therefore, HCGs are good candidates for this class of lasers, thanks to their broadband reflectivity, compactness and polarization features. In fact, DBRs are typically polarization-insensitive, while HCGs are highly-dichroic components that can assure a fixed polarization over the whole tuning range. A second application is related to on-chip silicon optical platforms. HCGs have been proposed [4], [5], [12], [13], because they can provide both the needed reflectivity.

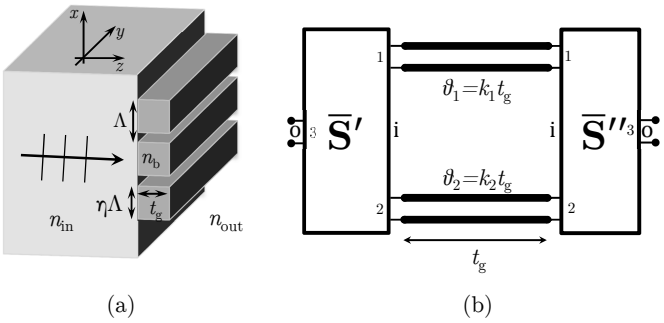

Fig. 1. **Left**: sketch of a high-contrast grating; the dielectric bars are characterized by refractive index $n_{\rm b}$, surrounded by an index $n_{\rm out}$ and lying on an index $n_{\rm in}$. The period Λ, filling factor η and thickness $t_{\rm g}$ are also defined. **Right**: equivalent circuit of a bimodal FPI. The scattering matrices of the left and right interfaces $\overline{\mathbf{S}}'$, $\overline{\mathbf{S}}''$ have two inner ports (i) and one outer port (o); the port labels are also indicated. The two inner ports are connected by two transmission lines with electrical lengths $\vartheta_1 = k_1 t_{\rm g}$ and $\vartheta_2 = k_2 t_{\rm g}$.

A HCG is a periodic structure composed of dielectric bars surrounded by air or deposited on a low-index material, as shown in Fig. 1(a). The higher is the refractive index contrast, the better is the mirror performance. The desired features appear in a well-defined wavelength region *i.e.,* the so-called "near-wavelength" regime [3]. In these conditions this structure lies between sub-wavelength gratings, which can be described by means of a polarization-dependent refractive index, and diffraction gratings having periods larger than the wavelength, which introduce diffracted orders. The near-wavelength regime does not lend itself to simplified approaches and requires an exact treatment. Several techniques have been proposed, which can be classified into two categories: "fully numerical approaches" and "modal methods". Examples of schemes belonging to the former class are finite differences, finite elements or spectral elements [14], [15], [16]. Fully numerical techniques are suitable for studying complex geometries, but they are rather demanding from a computational point of view. Moreover, they generally solve

Manuscript received August 23, 2018; revised October 11, 2018; accepted October 16, 2018.

A. Tibaldi, P. Debernardi and R. Orta are with the Consiglio Nazionale delle Ricerche (CNR), Istituto di Elettronica e di Ingegneria dell'Informazione e delle Telecomunicazioni (IEIIT), 10129 Turin, Italy. e-mail: alberto.tibaldi@ieiit.cnr.it

R. Orta is with the Department of Electronics and Telecommunications, Politecnico di Torino, Turin, 10129 Italy.

Maxwell's equations without providing so much information about the physics of the device, preventing from elaborating design strategies. On the other hand, in modal methods the electromagnetic field is represented as a superposition of the modes of a periodic waveguide, so that propagation along the longitudinal direction is described by closed-form expressions and the dimensionality of the numerical problem is reduced. The modes can be computed analytically [3], [17], by spectral methods [18], [19], [20] or by Fourier discretizations such as in the rigorous coupled wave analysis (RCWA) [21], [22], [23], [24], [25]. Even if modal methods cannot be applied to complex geometries they are quite fast, accurate, and allow to get deeper insight into the physical mechanisms occurring in the device.

Modal methods allow to intuitively understand the HCG operation in terms of the interference of two grating modes [26], [27], [3]. In view of providing rigorous foundations to this picture, Reference [28] proposes an analogy of HCGs with the generalized concept of Fabry-Pérot interferometer (FPI) sketched in Fig. 1(b). This framework has been applied to perform a complete characterization of the features of high/low-contrast grating high-Q resonators [29] by means of analytic expressions, showing explicit connections between Fano resonances (manifesting in quick zero-one transitions of the reflection coefficient), with leaky waves (related to the loop gain poles).

After presenting a narrow-band analysis in those two previous papers, this third work deals with the application of the analytic bimodal FPI framework to the description of HCG reflectors. Section II, after recalling the main results of [28], discusses the nature of the HCG broadband operation, proposes some design considerations for ultrabroadband HCG reflectors and a new HCG design approach. In Section III the generalized analytic expressions for asymmetric HCGs are provided, to which the same design scheme can be applied. For this case a discussion is provided about the constraints to be obeyed by the refractive index of the higher semi-infinite medium. Finally, Section IV deals with the application of the generalized FPI model to the analysis of lossy HCGs.

II. Symmetric HCG reflectors

Generally, the simplest way to design an HCG consists of the exploration of its parameter space by repeated analyses, performed by a mode-matching technique, such as RCWA. The HCG parameters are: wavelength (λ), grating period (Λ), filling factor (η, *i.e.,* ratio of the dielectric bar width to the period), and thickness (t_g). Actually, the grating features can be scaled by Λ, so that the parameter space reduces to three dimensions: $(\lambda/\Lambda, t_\mathrm{g}/\Lambda, \eta)$. In order to focus on a real device, Fig. 2 shows an example of parameter space exploration, inspired by the HCG studied in [3, Fig. 5]. This is illuminated by a TM plane-wave impinging perpendicularly to the grating plane. The map is drawn only in the bimodal range. The curved right boundary corresponds to the cutoff wavelengths of the second grating mode. The left boundary consists of a straight vertical segment plus an arc similar to the right one: the vertical segment, occurring at $\lambda = \Lambda$, indicates

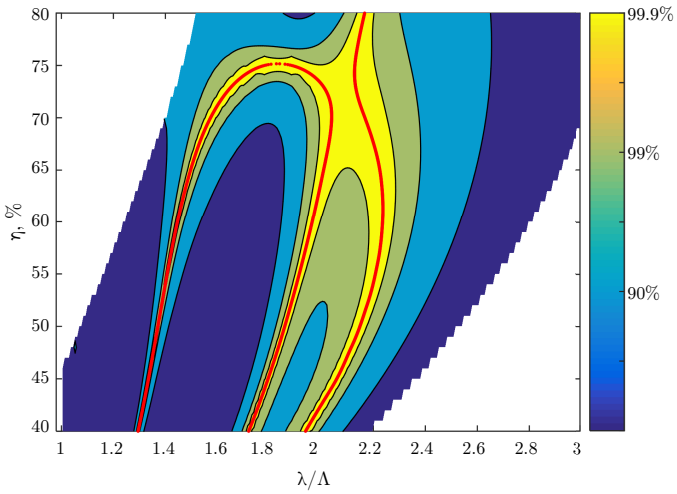

Fig. 2. $(\lambda/\Lambda, \eta)$ reflectivity map, in the bimodal operation region, of a symmetric high-contrast grating with bars ($n_\mathrm{b} = 3.214$) in air and $t_\mathrm{g} = 0.63\Lambda$. The yellow regions correspond to reflectivity greater than 99.9%. The red curve indicates the 100% reflectivity locus.

the cutoff of diffracting plane-waves in the outer half-spaces, while the curved one is related to the cutoff of the third grating mode. The curvature of these arcs is a consequence of the η-dependence of the grating dispersion features. Since one is interested in appreciating the details of very-high reflectivities, it is convenient to express it in terms of the "number of nines"

$$R^{(\#9)} = -\log_{10}(1 - |S_{11}|^2) = -\log_{10}|S_{21}|^2. \qquad (1)$$

This representation has been used to produce Fig. 2, where the yellow regions indicate reflectivity levels higher than 99.9%. Here, the red curves identify the 100% reflectivity loci. By performing the parametric analysis of Fig. 2 with different bar refractive indexes, it could be shown that the ultrabroadband high-reflectivity region lies always within the wavelength range exhibiting the same modal configuration, *i.e.,* two modes propagating in the grating and only the fundamental Floquet mode in the half-spaces. Therefore, just like HCG resonators [29], HCG reflectors can be effectively described as bimodal FPIs.

In view of exploiting the analogy between HCG reflectors and bimodal FPIs [28], it is useful to recall their main properties. As it can be seen in the sketch of Fig. 1, a bimodal FPI features two transmission lines with phase shifts ϑ_1, ϑ_2 in the FP cavity region, which represent the propagation of the two modes in the grating bars, and one access port in each outer region, describing homogeneous half-spaces. The inner and outer transmission lines are coupled by the 3×3 scattering matrices describing the bar junctions. If these junctions are assumed lossless and reciprocal, the corresponding scattering matrices are unitary and symmetric. This allows to parametrise the scattering matrix of the junction as [28]:

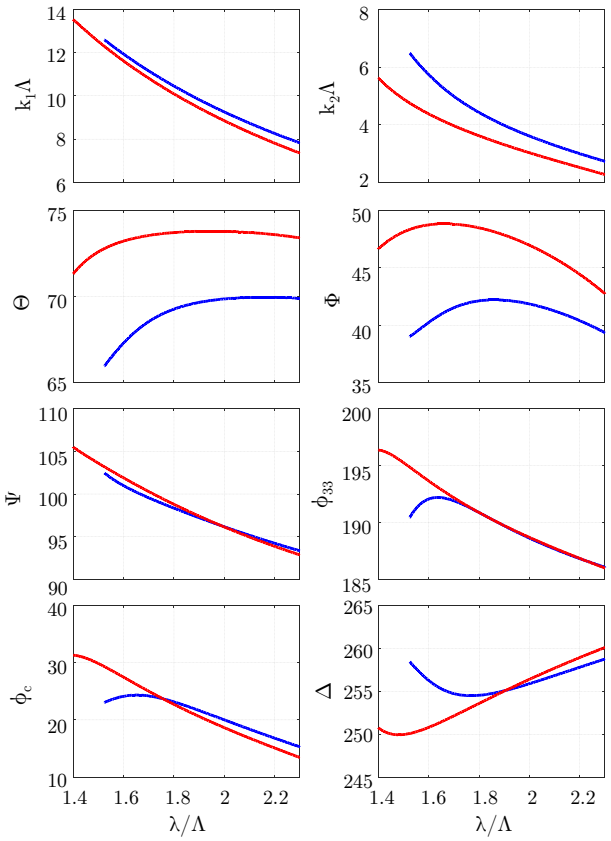

Fig. 3. Parameters of the bar-air junction for $\eta = 75\%$ and 62% (blue and red lines); $n_b = 3.214$. At the top, the normalized propagation constants and below the 6 parameters describing the 3×3 scattering matrix of the junction, obtained by applying the inverse formulas (3).

$$
\begin{aligned}
\overline{S}_{11} &= \mathrm{e}^{-\mathrm{j}(\varphi_c+\Delta)}\left[\mathrm{e}^{\mathrm{j}\Psi}\cos^2\Phi\cos\Theta - \mathrm{e}^{-\mathrm{j}\Psi}\sin^2\Phi\right]\\
\overline{S}_{22} &= \mathrm{e}^{-\mathrm{j}(\varphi_c-\Delta)}\left[\mathrm{e}^{-\mathrm{j}\Psi}\cos^2\Phi - \mathrm{e}^{\mathrm{j}\Psi}\sin^2\Phi\cos\Theta\right]\\
\overline{S}_{12} &= \frac{1}{2}\mathrm{j}\mathrm{e}^{-\mathrm{j}\varphi_c}\sin 2\Phi\left[\mathrm{e}^{-\mathrm{j}\Psi} + \mathrm{e}^{\mathrm{j}\Psi}\cos\Theta\right]\\
\overline{S}_{13} &= \mathrm{j}\mathrm{e}^{\mathrm{j}\frac{-\varphi_c+\varphi_{33}+\Psi}{2}}\mathrm{e}^{-\mathrm{j}\frac{\Delta}{2}}\sin\Theta\cos\Phi\\
\overline{S}_{23} &= -\mathrm{e}^{\mathrm{j}\frac{-\varphi_c+\varphi_{33}+\Psi}{2}}\mathrm{e}^{\mathrm{j}\frac{\Delta}{2}}\sin\Theta\sin\Phi\\
\overline{S}_{33} &= \mathrm{e}^{\mathrm{j}\varphi_{33}}\cos\Theta.
\end{aligned}
\tag{2}
$$

Starting from nine complex coefficients in the general case, this parametrization represents the manifold of unitary symmetric matrices with six real numbers, three angles and three phases. The angles have a simple physical meaning. Θ and Φ quantify the coupling between the diffraction order and the two modes in the bar, Ψ describes the coupling of the two modes at the interfaces. For example, focusing on $\overline{S}_{33}$, $\Theta = 90°$ corresponds to transmitting the whole power to the inner ports, leading to no reflection at the junction. Considering $\overline{S}_{13}$ and $\overline{S}_{23}$, $\Phi = 0°$ and $90°$ correspond to coupling all the power to the first or to the second port on the cavity side, whereas $\Phi = 45°$ corresponds to equal power splitting.

One of the remarkable features of this parametrization compared to others present in the literature [30], [31], [32], is the availability of simple inverse formulas:

$$
\begin{aligned}
\Theta &= \arccos(|\overline{S}_{33}|)\\
\varphi_{33} &= \arg\left(\overline{S}_{33}\right)\\
\Phi &= \arccos\left(\frac{|\overline{S}_{13}|}{\sin\Theta}\right) = \arcsin\left(\frac{|\overline{S}_{23}|}{\sin\Theta}\right)\\
\varphi_c &= -\frac{1}{2}\arg\left(\frac{\overline{S}_{11}\overline{S}_{22} - \overline{S}_{12}^2}{\cos\Theta}\right)\\
\Delta &= (\arg(\overline{S}_{23}) - \arg(\overline{S}_{13})) - \frac{\pi}{2}\\
\Psi &= \arg(\overline{S}_{23}) + \arg(\overline{S}_{13}) + \varphi_c - \varphi_{33} - \frac{3\pi}{2}.
\end{aligned}
\tag{3}
$$

In Fig. 3 the six parameters obtained applying the inverse formulas (3) to the junction scattering coefficients are shown for some grating geometries. All the junction angles are slowly varying functions of both the wavelength and filling factor and span limited angular ranges.

This parametrization is the added value of this approach, as it can be exploited to derive explicit expressions for the bimodal FPI response. It is useful to rewrite from [28] the explicit expression of S_{21}:

$$
S_{21} = \frac{N}{D}\mathrm{e}^{-\mathrm{j}\tau}\mathrm{e}^{\mathrm{j}\varphi_{33}}, \tag{4}
$$

where:

$$
D = c_{4\mathrm{d}}\mathrm{e}^{-\mathrm{j}4\tau} + c_{2\mathrm{d}}\mathrm{e}^{-\mathrm{j}2\tau} + 1, \tag{5}
$$

and

$$
\begin{aligned}
c_{4\mathrm{d}} &= \cos^2\Theta\\
c_{2\mathrm{d}} &= \mathrm{e}^{-\mathrm{j}(2\Psi+2\delta)}\left(p_4\mathrm{e}^{\mathrm{j}4\Psi} + p_2\mathrm{e}^{\mathrm{j}2\Psi} + p_0\right),
\end{aligned}
$$

and

$$
\begin{aligned}
p_4 &= -\cos^2\Theta\left(\cos^2\Phi - \mathrm{e}^{2\mathrm{j}\delta}\sin^2\Phi\right)^2\\
p_2 &= \frac{1}{2}\left(1 + \mathrm{e}^{2\mathrm{j}\delta}\right)^2\cos\Theta\sin^2 2\Phi\\
p_0 &= -\left(\sin^2\Phi - \mathrm{e}^{2\mathrm{j}\delta}\cos^2\Phi\right)^2,
\end{aligned}
$$

where the equivalent transmission line propagation terms are defined as

$$
\tau = \frac{k_1 + k_2}{2}t_g + \varphi_c \tag{6}
$$

$$
\delta = \frac{k_1 - k_2}{2}t_g + \Delta. \tag{7}
$$

Even if these quantities have no strong physical meaning, they are convenient variables to work with. As for the reflection coefficient magnitude, the only parameter investigated in this paper, one can rely on (1); for the complete expression, refer to eq.(24) of [28].

The numerator N in (4) is given by

$$
N = -\frac{1}{2}\mathrm{e}^{-\mathrm{j}(\Psi+\delta)}\sin^2\Theta\left(c_{0\mathrm{n}} + c_{1\mathrm{n}}\mathrm{e}^{-\mathrm{j}2\tau}\right), \tag{8}
$$

with

$$
\begin{aligned}
c_{0\mathrm{n}} &= \mathrm{e}^{\mathrm{j}2\Psi}\left(1 - \mathrm{e}^{2\mathrm{j}\delta} + \left(1 + \mathrm{e}^{2\mathrm{j}\delta}\right)\cos 2\Phi\right)\\
c_{1\mathrm{n}} &= \left(1 - \mathrm{e}^{2\mathrm{j}\delta}\right) - \left(1 + \mathrm{e}^{2\mathrm{j}\delta}\right)\cos 2\Phi.
\end{aligned}
$$

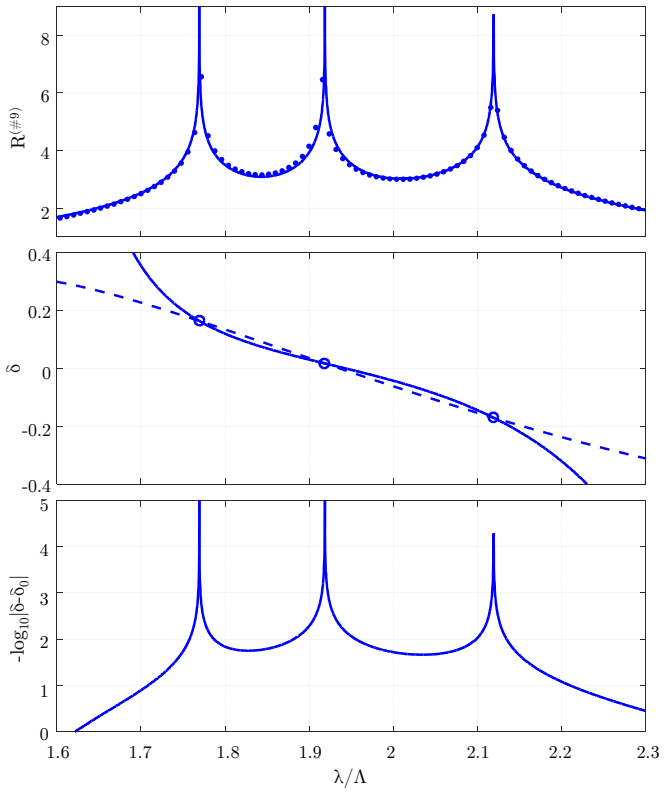

Fig. 4. Symmetric bars-in-air grating with $n_{\mathrm{b}} = 3.214$, $t_{\mathrm{g}} = 0.632\Lambda$ and $\eta = 75\%$. **Top**: reflectivity spectrum. **Center**: δ computed with (7) (dashed curve) and δ_0 computed with (9) (solid curve). **Bottom**: $|\delta - \delta_0|$ in logarithmic scale.

After manipulating (8), it is possible to prove that a transmission zero occurs when the condition

$$\delta_0 = \arctan\left[\tan\left(\tau + \Psi\right)\cos 2\Phi\right] \tag{9}$$

is satisfied. It is to be pointed out that the position of transmission zeros does not depend on the in/out coupling at the junction Θ, but it is affected by the power partition between the two grating modes, Φ. This is interesting since, as shown in Fig. 3, HCG reflectors operate in the proximity of this condition.

In order to apply this model to the description of ultrabroadband HCG reflectors, it is necessary to relieve the hypothesis of absence of dispersion introduced in [28], [29] for the junction parameters. In particular, in these works δ was assumed frequency-independent as well. Even if this assumption is locally acceptable, for instance in view of characterizing narrowband resonance phenomena, it may generate misleading results when applied over broad wavelength ranges. For example, [28] states that a single transmission zero always occurs, for constant δ, by varying τ in the $[0, \pi]$ range. This statement seems to contradict the results published in the literature, which show two 100% reflectivity peaks. This is very important because the presence of multiple, neighboring peaks is at the basis of broadband operation.

A striking example is reported in Fig. 4 (top), which shows a HCG reflectivity spectrum exhibiting three 100% reflectivity peaks. It is to be remarked that the reflectivity remains very high (above 99.9%) also in the valleys between them. If the actual frequency dependence of both the junction parameters (3) and the transmission line propagation terms (6), (7) is taken into account, the bimodal FPI model can reproduce accurately the broadband operation of an HCG reflector, as demonstrated in Fig. 4 (top). There, the solid curve exhibits a remarkable agreement with the RCWA results (dot markers). For the sake of generality, in this paper results are reported versus normalized wavelenghts and refractive index dispersion has not been included. In fact, it would just provide minor shifts to the peaks, without adding much to the device behavior. However, material dispersion could be kept into account at no extra computational cost in the preliminary RCWA simulations when choosing a specific wavelength operation range. In other words, starting from the one-peak picture of [28], the presence of multiple peaks can be interpreted as the "wavelength shift" of this single peak, caused by dispersion. This is the first time, to the best of our knowledge, that the origin of multiple reflectivity peaks is explained.

To deepen this perspective, Fig. 4 (center) reports two curves: the solid one, obtained by (9) and (6), and the dashed one, from (7). The solid curve is the locus of $(\lambda/\Lambda, \delta_0)$ points such that 100% reflectivity occurs. However, it does not include complete information about the propagation (k_1, k_2) occurring in the grating, which is instead included in the dashed curve. Then, transmission zeros occur at the intersections of these two curves, indicated by circular markers.

To summarize, in the former approach presented in [28], [29], the effect of dispersion was included only in τ, so that δ_0 was a monotonic function and δ a constant, leading to the fact that only one peak was observed. In actual devices, all parameters depend on wavelength, therefore dispersion influences both the dashed curve δ, which becomes a function of λ, and the solid curve δ_0, which could be non-monotonic. As emphasized by the extraordinary agreement between the intersections of the dashed/solid curves, indicated by circular markers, this representation allows to describe, by means of a simple analytic expression, the operation of high-contrast grating reflectors.

One added value of the curves reported in Fig. 4 (center) is the achievement of a qualitative estimate of the transmission coefficient in the intervals between the reflection peaks. In fact, Fig. 4 (bottom) shows the difference $\delta - \delta_0$ in logarithmic scale. This is quite similar to the reflection coefficient in the top plot, proving that the closer the δ and δ_0 curves are, the higher is the reflectivity. In other words, if it could be possible to find a configuration such that $\delta = \delta_0$ in a wavelength range, then the HCG would exhibit 100% reflection on it. Therefore, by simply inspecting this quantity, one can find the best parameter combinations for broadband operation.

The analysis based on the δ and δ_0 curves allows to classify different HCG operation regimes, which can be useful in view of establishing new design guidelines based on the bimodal FPI concept. To this aim, Fig. 5 reports the reflectivity spectra (top) and the corresponding δ, δ_0 curves (bottom) for two gratings characterized by $n_{\mathrm{b}} = 3.214$ (the same of Fig. 4), with $\eta = 62\%$. The blue curves are obtained for a grating very similar to that of [3, Fig. 5(a)] (with $t_{\mathrm{g}} = 0.63\Lambda$), featuring

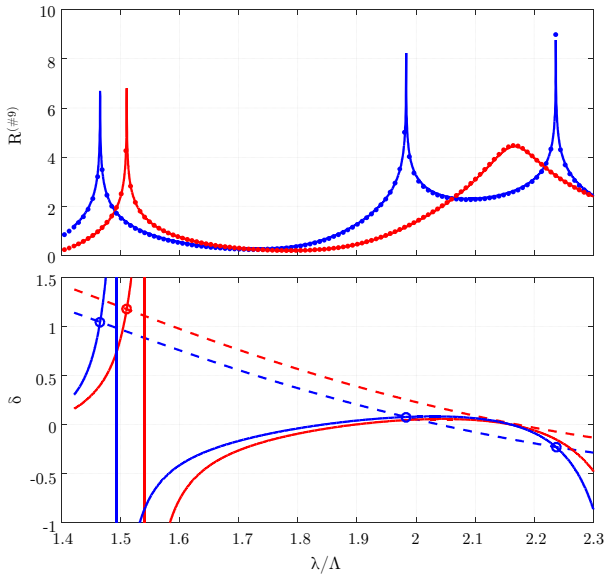

Fig. 5. **Top**: reflection coefficient in number of 9 for a HCG with $n_{\rm b} = 3.214$, $\eta = 62\%$ and $t_{\rm g} = 0.63\Lambda$ (blue, same as [3] Fig. 5) and $t_{\rm g} = 0.66\Lambda$ (red); dots refer to full RCWA computation. **Bottom**: as in Fig. 4, center.

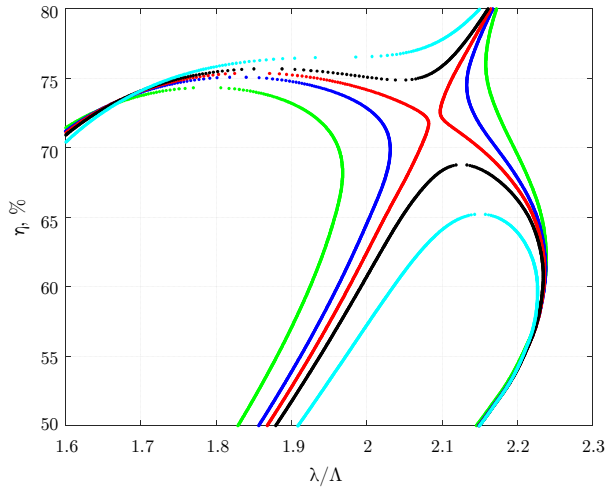

Fig. 6. 100% reflectivity loci in the symmetric configuration, for gratings with $n_{\rm b} = 3.214$, and $t_{\rm g} = 0.619\Lambda$ (green), 0.629Λ (blue), 0.633Λ (red), 0.637Λ (black) and 0.647Λ (cyan). Compared to Fig. 2, the loci are zoomed in the region of interest.

the common "double peak".

Even if both the gratings corresponding to the blue reflectivity curve of Fig. 5 and to that of Fig. 4 exhibit three peaks, they belong to two families, which differ for the peak spacings. This difference is evident when comparing Figs. 4(center) and 5(bottom): in the former the dashed and solid curves are very close to each other over a broad range, leading to a very large bandwidth. On the other hand, in the latter the presence of the discontinuity causes one peak to be far from the other two.

Since the dispersion curves $\delta(\lambda)$ (from (7)) are always monotonic decreasing, the classification arises from the different behaviors of the 100% reflection loci δ_0. In fact, in Fig. 5 the δ_0 curve exhibits a change of slope around $\lambda = 2.1\Lambda$. The origin of this is clear from (9) and the red Φ curve of Fig. 3. Indeed, the change of slope corresponds to the $\Phi = 45°$ crossing. On the other hand, the blue Φ curve does never cross $\Phi = 45°$, causing the δ_0 curve from Fig. 4 to be monotonic. As Φ rules the power balance between the two grating modes, having $45°$ crossings corresponds to a switch of the dominant mode. In addition to avoiding mode switching, in order to obtain a large bandwidth, it is required for the slopes of the δ and δ_0 curves to be similar, so that the best condition is $\Phi < 45°$.

As a final example, the red curve of Fig. 5 (obtained for $t_{\rm g} = 0.66\Lambda$) exhibits an interesting behavior: even if no intersections of the δ and δ_0 curves occur in the two-peak region, reflectivity reaches high values because, what does matter is their proximity, as already discussed for Fig. 4 (bottom).

In order to draw some design considerations relying on the bimodal FPI concept, a fundamental step is to produce a synthetic representation of the reflectivity features on the whole 3-D parameter space. To this aim, Fig. 6 reports the 100% reflectivity loci, as also shown in Fig. 2 for only one $t_{\rm g}$ value, on the $(\lambda/\Lambda, \eta)$ plane, for various values of grating thickness. Therefore, this plot represents the evolution, with respect to the $t_{\rm g}$ parameter, of the 100% reflectivity loci. Drawing each locus would require to search, for each η value, the HCG transmission zero by means of a root-finding algorithm, so that a huge number of RCWA computations should be performed. By exploiting the bimodal FPI expressions, these loci are found in a quick and efficient way by a coarse sampling of the $(\lambda/\Lambda, \eta)$ plane of the junction parameters and propagation constants. Then, such profiles, which appear to be always smooth (see Figs. 3), are interpolated on a much denser grid at almost zero numerical effort. The availability of interpolated parameters to be used in simple analytic formulas allows to compute efficiently such loci as the intersections of the δ and δ_0 curves of Figs. 4, 5.

The aforementioned two HCG reflector families correspond to two different design concepts, which can be both investigated by the synthetic representation of Fig. 6. In fact, a "classic" two-peaks HCG can be designed by choosing the thickness corresponding to the transmission zeros having optimal relative distance (designed from a trade-off of desired reflectivity level and bandwidth), and the filling factor η by cutting with an horizontal line the desired section. This design is quite robust against variations of both $t_{\rm g}$, which will just change the relative distance of the transmission zeros, and η. A different aim could be that of looking for regions where the transmission zero loci exhibit zero derivative. This goal may recall the guideline proposed in [17]. In fact, by cutting with an η=constant line such region, the reflectivity would be very high over an ultra-broad band. This is how the design presented in Fig. 4 has been obtained: the quasi-horizontal transmission zero loci are, in fact, mapped into $\delta \simeq \delta_0$ curves.

III. Asymmetric HCG reflectors

The previous ideas can be easily extended to the asymmetric case, which is of interest for more manufacture-oriented mirrors. For an asymmetric FPI, by denoting the left and right

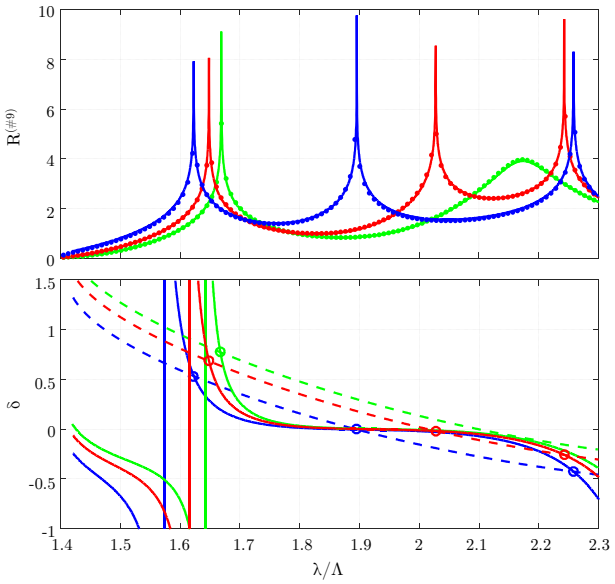

Fig. 7. **Top**: reflectivity of an asymmetric HCG with $n_{\rm in} = 1.41$, $n_{\rm b} = 3.214$, $\eta = 62\%$ and $t_{\rm g} = 0.63\Lambda$ (blue), $t_{\rm g} = 0.66\Lambda$ (red) and $t_{\rm g} = 0.68\Lambda$ (green); dots refer to full RCWA computation, the solid curve to the bimodal FPI model. **Bottom**: as in Fig. 4, center.

junction by the superscripts a, b and introducing the equivalent parameters

$$\tau = \frac{k_1 + k_2}{2} t_{\rm g} + \frac{\varphi_{\rm c}^{\rm a} + \varphi_{\rm c}^{\rm b}}{2}$$
$$\overline{\Psi} = \frac{\Psi^{\rm a} + \Psi^{\rm b}}{2}$$
$$\delta = \frac{k_1 - k_2}{2} t_{\rm g} + \frac{\Delta^{\rm a} + \Delta^{\rm b}}{2}, \qquad (10)$$

it can be proved that the transmission zero condition (9) becomes

$$\delta_0 = \arctan\left(\frac{\cos(\Phi^{\rm a} + \Phi^{\rm b})}{\cos(\Phi^{\rm a} - \Phi^{\rm b})} \tan\left(\tau + \overline{\Psi}\right) \right). \qquad (11)$$

As an example, Fig. 7 reports a set of results analogous to those of Fig. 5, but for dielectric bars laid on an oxide substrate. It can be seen that there is no apparent drawback in placing high index bars on a lower index substrate, until it continues to support just one propagating order. In fact, the impact of the substrate index on the junction parameters can be appreciated in Figs. 8 and 9. In most cases the variations of the parametrization angles evaluated by (3) are stronger, the lower is the index contrast. Moreover, the bandwidth appears to be narrower due to the closer cutoff of the diffracted orders in the oxide, as emphasized by the long vertical boundary at $\lambda = 1.41\Lambda$ (due to the corresponding $n_{\rm in} = 1.41$). This shrinks the bimodal FPI operation region, as well as the corresponding high-reflectivity broadband operation range, until reaching the monolithic HCG (MHCG) limit [6], [33]. Due to the presence of multiple diffracted orders in the substrate, MHCGs do not belong to the class of devices described in the present paper.

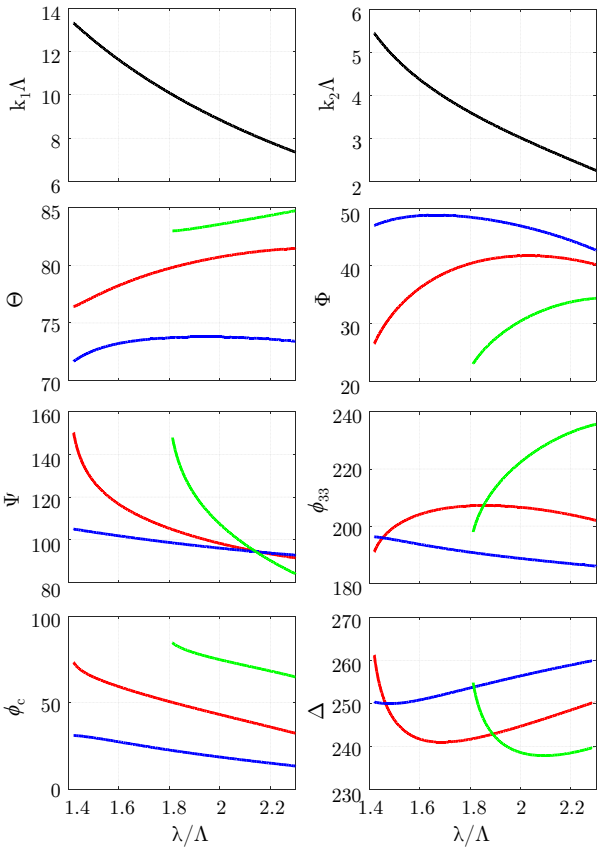

Fig. 8. Parameters of the bar-air (blue lines) and of the bar-substrate ($n_{\rm in}$ =1.41 and 1.80, red and green lines respectively) junctions for $\eta = 62\%$. At top, the normalized propagation constants and below the 6 angles describing the 3x3 scattering matrix of the junction, obtained by applying the inverse formulas (3).

By comparing the zero transmission loci of symmetric and asymmetric HCGs (Figs. 6 and 9) useful information can be gained:

- the broadband HCG region of interest is limited from below to $\lambda/\Lambda = n_{\rm in}$,
- the symmetric and asymmetric mirrors loci are obtained by changing the HCG thickness within 4.3% (from 0.619Λ to 0.647Λ) and 2.5% (from 0.662Λ to 0.6795Λ) relative ranges respectively, leading to quite similar evolution plots; this indicates that the sensitivity of the HCG performance with respect to its thickness is higher in the asymmetric case.
- the bandwidth of the asymmetric HCG is reduced and the sensitivity to filling factor increased.

IV. Accounting for the Presence of Losses

The analysis approach based on the bimodal FPI model has been derived assuming to deal with lossless materials. In this section, we show that the model can be applied also to the more realistic case of lossy gratings. The idea is that the loss in the bulk of the bars plays a major role in comparison with that related to the interfaces. Hence, one can use the scattering matrices of the interfaces evaluated for the same grating but neglecting the losses, accounting for them only in the transmission lines describing the propagation of the modes

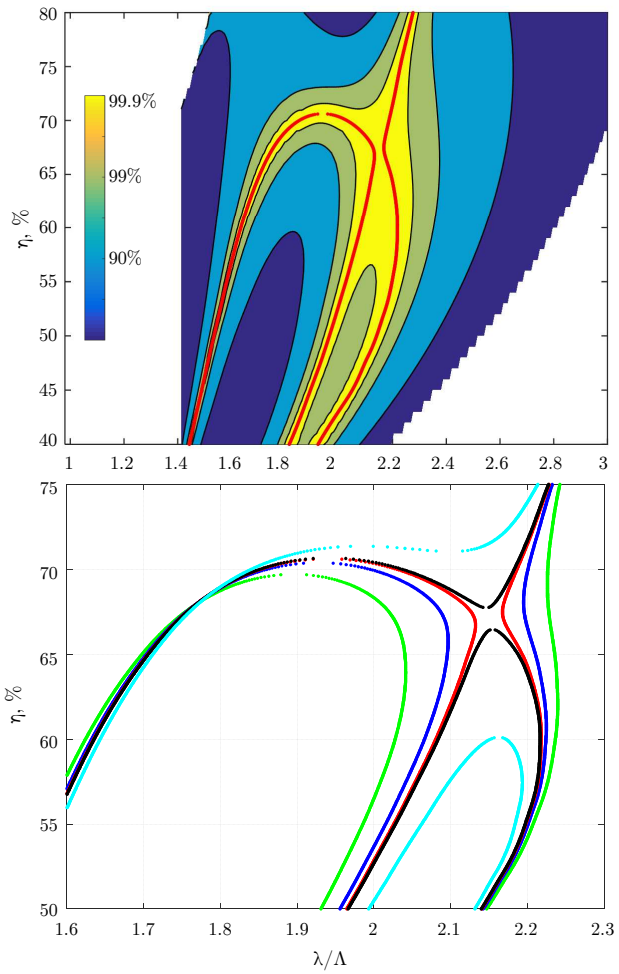

Fig. 9. **Top**: Reflectivity map in the bimodal operation region of an asymmetric HCG with $n_{\rm in} = 1.41$, bar $n_{\rm b} = 3.214$ and $t_{\rm g} = 0.672\Lambda$ in the $\lambda/\Lambda - \eta$ plane. The yellow regions correspond to reflectivity greater than 99.9%. The red curve indicates the 100% reflectivity locus. **Bottom**: HCG as above, but showing the 100% reflectivity loci for different thickness: $t_{\rm g} = 0.662\Lambda$ (green), 0.6695Λ (red), 0.672Λ (red), 0.6725Λ (black) and 0.6795Λ (cyan). The loci are zoomed in the region of interest and in the same range of Fig.6 for an easier comparison.

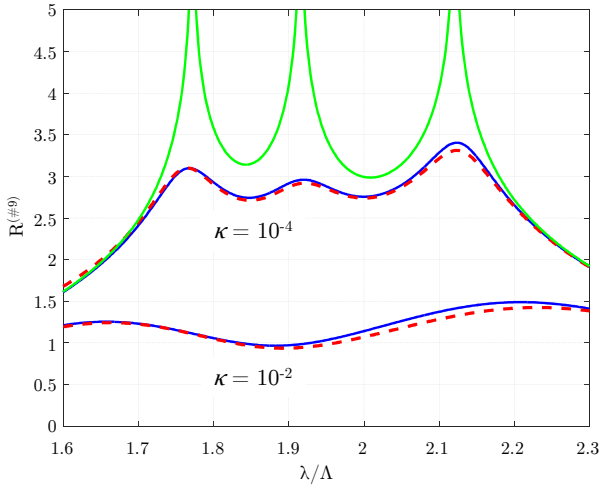

Fig. 10. Reflectivity of the grating of Fig. 4. The blue and red curves are obtained for lossy gratings with RCWA and with the generalized FPI model. The results are reported for two amounts of losses, characterized by the extinction coefficient κ. The lossless case is shown for reference in green.

in the grating bars. This concept is tested in Fig. 10, where the grating of Fig. 4 is analyzed by including losses both in the full RCWA and in the bimodal FPI approach. Good agreement is achieved independently of the amount of loss, demonstrating the small influence of the slight non-unitarity of the interface scattering matrix on the grating reflection coefficient. It is to be remarked that, in presence of reasonable losses, the general structure of the response is unchanged with respect to the lossless case, so that this can still be used for design purposes. On the contrary, very high losses drastically modify the response, and the corresponding low reflectivity makes this device no longer useful.

V. Conclusions

Due to their bimodal principle of operation, high-contrast gratings can be modeled as generalized Fabry-Pérot interferometers [28]. Previously [29] such description allowed to study HCG resonators from a new perspective, deepening our understanding of narrowband features such as Fano resonances.

This work focuses on HCGs as broadband reflectors and shows that dispersion is the key mechanism generating the 100% reflectivity multiple peaks and the corresponding high-reflectivity regions between them. The simple analytic expressions for the 100% reflectivity condition have been applied to analyze broadband operation for both the symmetric and asymmetric cases. New design guidelines for ultrabroadband HCG reflectors, to some extent complementary to those of [17], have been proposed, resulting in simple qualitative/quantitative analytical expressions, suited to investigate also the design sensitivity. Even if developed under the assumption of lossless structures, this model proved to be effective for realistic gratings as well.

Beyond providing rigorous explanations and interpretations of the grating physics, the bimodal FPI framework can be exploited for HCG design. As it can be seen in Fig. 3 and 8, in the cases of interest the junction parameters are mildly dispersive. For this reason, it is possible to evaluate such parameters by a full-wave approach only at few wavelengths and filling factors. This allows to perform in few seconds extensive parameter space explorations.

References

[1] C. J. Chang-Hasnain, Y. Zhou, M. C. Y. Huang, and C. Chase, "High-contrast grating VCSELs," *IEEE J. Sel. Topics Quantum Electron.,* vol. 15, no. 3, May/June 2009.

[2] Y. Zhou, M. C. Y. Huang, C. Chase, V. Karagodsky, M. Moewe, B. Pesala, F. G. Sedgwick, and C. J. Chang-Hasnain, "High-index contrast grating (HCG) and its applications in optoelectronic devices," *J. Sel. Topics Quantum Electron.,* vol. 15, no. 5, pp. 1485-1499, Sept./Oct. 2009.

[3] C. J. Chang-Hasnain and W. Yang, "High-contrast gratings for integrated optoelectronics," *Adv. Opt. Photon.,* vol. 4, pp. 379-440, 2012.

[4] C. Sciancalepore, B. B. Bakir, S. Menezo, X. Letartre, D. Bordel, and P. Viktorovitch, "III-V-on-Si photonic crystal vertical-cavity surface-emitting laser arrays for wavelength division multiplexing," *IEEE Photon. Technol. Lett.,* vol. 25, no. 12, pp. 1111-1113, June 2013.

[5] A. Liu, W. Hofmann, and D. H. Bimberg, "Two-dimensional analysis of finite size high-contrast gratings for applications in VCSELs," *Opt. Express,* vol. 22, no. 10, pp. 11804-11811, May 2014.

[6] M. Gebski, M. Dems, A. Szerling, M. Motyka, L. Marona, R. Kruszka, D. Urbańczyk, M. Walczakowski, N. Palka, A. Wójcik-Jedlińska, Q. J. Wang, D. H. Zhang, M. Bugajski, M. Wasiak, and T. Czyszanowski, "Monolithic high-index contrast grating: a material independent high-reflectance VCSEL mirror," *Opt. Express,* vol. 23, no. 9, pp. 11674-11686, May 2015.

[7] I.-S. Chung, "Study on differences between high contrast grating reflectors for TM and TE polarizations and their impact on VCSEL designs," *Opt. Express,* vol. 23, no. 13, pp. 16730-16739 Jun. 2015.

[8] R. Michalzik, "VCSELs - Fundamentals, technology and applications of vertical-cavity surface-emitting lasers," *Springer Series in Optical Sciences,* Springer-Verlag, vol. 166, Berlin Heidelberg, 2013.

[9] D. D. John, C. B. Burgner, B. Potsaid, M. E. Robertson, B. K. Lee, W. J. Choi, A. E. Cable, J. G. Fujimoto, V. Jayaraman, "Wideband electrically-pumped 1050 nm MEMS-tunable VCSEL for ophthalmic imaging," *J. Lightwave Technol.,* vol. 33, no. 6, pp. 3461-3468, Aug. 2015.

[10] C. Gierl, T. Gründl, P. Debernardi, K. Zogal, C. Grasse, H. A. Davani, G. Böhm, S. Jatta, F. Küppers, P. Meißner, and M. C. Amann, "Surface micromachined tunable 1.55 μm-VCSEL with 102 nm continuous single-mode tuning," *Optics Express,* vol. 19, no. 18, pp. 17336-17343, Aug. 2011.

[11] M. C. Y. Huang, Y. Zhou, and C. J. Chang-Hasnain, "A surface-emitting laser incorporating a high-index-contrast subwavelength grating," *Nature Photonics,* vol. 1, pp. 119-122, Feb. 2007.

[12] S. Learkthanakhachon, A. Taghizadeh, G. C. Park, K. Yvind, and I.-S. Chung, "Hybrid III-V/SOI resonant cavity enhanced photodetector," *Opt. Exp.*, vol. 24, no. 15, pp. 16512-16519, 2016.

[13] A. Taghizadeh, J. Mørk, I.-S. Chung, "Numerical investigation of vertical cavity lasers with high-contrast gratings using the Fourier modal method," *J. Lightwave Technol.*, vol. 34, no. 18, pp. 4240-4251, 2016.

[14] A. Taflove and S. C. Hagness, "Computational electrodynamics: the finite-difference time-domain method," *Artech House Antennas and Propagation Library*, Artech House, III edition, 2013.

[15] G. Pelosi, A. Freni, and R. Coccioli, "Hybrid technique for analysing scattering from periodic structures," *IEE Proceedings H,* vol. 140, no. 2, pp. 65-70, Apr. 1993.

[16] A. Tibaldi, R. Orta, O. A. Peverini, G. Addamo, G. Virone, and R. Tascone, "Skew incidence plane-wave scattering from 2-D dielectric periodic structures: analysis by the mortar-element method," *IEEE Trans. Microw. Theory Techn.,* vol. 63, no. 1, pp. 11-19, Jan. 2015.

[17] V. Karagodsky, F. G. Sedgwick, and C. J. Chang-Hasnain, "Theoretical analysis of subwavelength high contrast grating reflectors," *Opt. Express,* vol. 18, no. 16, pp. 16973-16988, Aug. 2010.

[18] R. H. Morf, "Exponentially convergent and numerically efficient solution of Maxwell's equations for lamellar gratings," *J. Opt. Soc. Am. A,* vol. 12, no. 5, pp. 1043-1056, May 1995.

[19] R. Orta, S. Bastonero and R. Tascone, "Numerical analysis of surface relief gratings", *Diffractive Optics and Optical Microsystems,* S. Martellucci and A. Chester Eds., pp. 47-56, Plenum Press, New York, USA, 1997.

[20] S. Bastonero, O. A. Peverini, R. Orta and R. Tascone, "Anisotropic surface relief diffraction gratings under arbitrary plane wave incidence", *Optical and Quantum Electronics*, vol. 32, pp. 1013-1025, 2000

[21] M. G. Moharam and T. K. Gaylord, "Rigorous coupled-wave analysis of planar-grating diffraction," *J. Opt. Soc. Am.,* vol. 71, no. 7, pp. 811-818, July 1981.

[22] L. Li, "Use of Fourier series in the analysis of discontinuous periodic structures," *J. Opt. Soc. Am. A.,* vol. 13, no. 9, pp. 1870-1876, Sep. 1996.

[23] M. Dems, R. Kotynski, and K. Panajotov, "PlaneWave Admittance Method - a novel approach for determining the electromagnetic modes in photonic structures," *Opt. Express,* vol. 13, no. 9, pp. 3196-3207, 2005

[24] P. Debernardi, R. Orta, T. Gründl, and M. C. Amann, "3-D vectorial optical model for high-contrast grating vertical-cavity surface-emitting lasers," *IEEE J. Quantum Electron.,* vol. 49, no. 2, pp. 137-145, Feb. 2013.

[25] A. Tibaldi, P. Debernardi, and R. Orta "High-contrast gratings performance issues in tunable VCSELs," *IEEE J. Quantum Electron.* vol. 51, no. 12, Dec. 2015.

[26] R. Magnusson and M. Shokooh-Saremi, "Physical basis for wideband resonant reflectors," *Opt. Express,* vol. 16, no. 5, pp. 3456-3462, Feb. 2008.

[27] V. Karagodsky, C. Chase, and C. J. Chang-Hasnain, "Matrix Fabry-Pérot resonance mechanism in high-contrast gratings," *Opt. Lett.,* vol. 36, no. 9, pp. 1704-1706, Apr. 2011.

[28] R. Orta, A. Tibaldi, and P. Debernardi, "Bimodal resonance phenomena. Part I: generalized Fabry-Pérot interferometers," *IEEE J. Quantum Electron.,* vol. 52, no. 12, pp. 6100508, Oct. 2016.

[29] R. Orta, A. Tibaldi, and P. Debernardi, "Bimodal resonance phenomena. Part II: high/low-contrast grating resonators," *IEEE J. Quantum Electron.,* vol. 52, no. 12, pp. 6600409, Oct. 2016.

[30] P. Dita, "Parametrisation of unitary matrices," *J. Phys. A: Math. Gen.,* vol. 15, pp. 3465-3473, 1982.

[31] C. Jarlskog, "A recursive parametrization of unitary matrices," *J. Math. Phys.,* vol. 46, pp. 103508, Oct. 2005.

[32] C. Jarlskog, "Recursive parametrization and invariant phases of unitary matrices," *J. Math. Phys.,* vol. 47, pp. 013507, Jan. 2006.

[33] M. Dems, "Monolithic high-contrast gratings: why do they not scatter light?," *J. Lightwave Technol.*, vol. 35, pp. 159-165, 2016.

Alberto Tibaldi was born in Casale Monferrato, Italy, in 1987. In 2009, 2011 and 2015 he received the B.Sc., M.Sc. and Ph.D. degrees in Electronic Engineering from Politecnico di Torino. In 2012 he joins the Italian National Council of Research (CNR) as a research fellow. Currently he teaches courses on numerical analysis and semiconductor device simulation. His scientific interests mainly regard the electrical and optical modeling of photonic devices.

Pierluigi Debernardi was born in Casale Monferrato and received his degree in Electronics Engineering in 1987 from Politecnico di Torino, Italy. Since 1989 he's with the Italian National Council of Research at Politecnico di Torino. His interests are mainly in the field of the modeling of semiconductor materials and devices for optoelectronic applications. Recently he is mostly involved in modeling and designing VCSEL structures with non-circular and/or complex geometries, so as to achieve specific performances.

Renato Orta (M'92-SM'99) is a member of the Department of Electronics, Politecnico di Torino, since 1974. He joined the Department as Assistant Professor in 1981, in 1987 became Associate Professor and since 1999 is Full Professor. He currently teaches courses on electromagnetic field theory and optical components. His research interests include the areas of microwave and optical components, radiation and scattering of waves and numerical techniques. He is Senior Member of the IEEE.